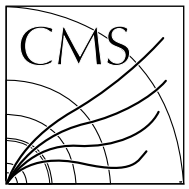

The Compact Muon Solenoid Experiment

CMS Note

Mailing address: CMS CERN, CH-1211 GENEVA 23, Switzerland

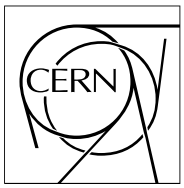

5 November 1999

Monte Carlo studies of the CMS Electromagnetic Endcap Calorimeter

B. W. Kennedy

Rutherford Appleton Laboratory,
Chilton, Didcot, Oxfordshire, GB

Abstract

Various design options for the Electromagnetic Endcap Calorimeter have been simulated in GEANT to assess their impact on the physics performance of the detector. The crystal size and spacing, the inter-module spacing, the structural material used for the modules, and the nature of the pointing geometry have all been varied, and the calorimeter response evaluated.

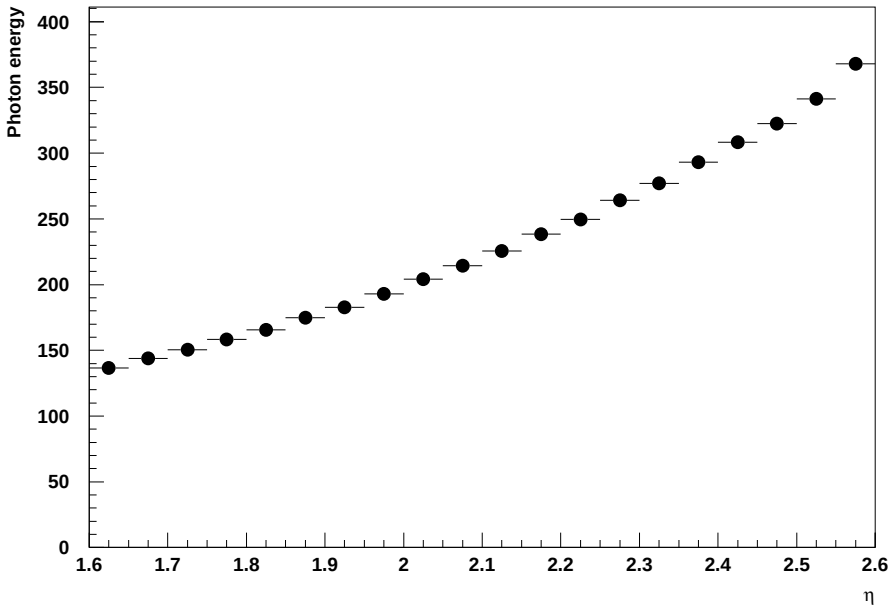

Figure 1: Variation of beam energy with rapidity for endcap simulation.

1 Introduction

The design of the electromagnetic calorimeter naturally represents a compromise between the desire to optimise the performance and the financial and other resources available to construct the detector. This note describes a series of Monte Carlo studies to assess the effect of various design features on the physics response of the calorimeter.

It is impossible to avoid the presence of gaps between the crystals, potentially degrading the calorimeter performance. The effect of such gaps is investigated in section 3. Similarly, the spaces between modules (known as "supercrystals") can have an adverse effect on performance if they become too large. This is explored in section 4. These inter-supercrystal spaces are known as "cracks", as this term has been used to describe the inter-module spaces in the barrel [1].

At the time of writing there is an active debate within the collaboration about the optimum size of the endcap crystals. Costs can be reduced by using shorter crystals (thereby reducing the amount of material), and by increasing the cross-section (to reduce the number of electronics channels). Section 5 presents results on the physics impact of both of these strategies.

Section 6 shows the effect on the calorimeter performance of different materials which might be used to construct the alveolar container.

The CMS endcaps have a quasi-pointing geometry, in which the crystals converge to a focal point some distance away from the interaction region at the centre of the detector. The choice of this off-pointing distance is discussed in section 7.

The two-photon decay process H$\rightarrow\gamma\gamma$ for a Higgs boson of mass close to 100GeV is regarded as a crucial benchmark in evaluating the performance of the CMS electromagnetic calorimeter. This decay mode will generate photons with a typical transverse momentum $p_T = 50$GeV. In the simulations reported here, photons were fired into the endcap with just this p_T: consequently their energy varies as a function of rapidity, as shown in figure 1. The photons were distributed uniformly over the rapidity range from 1.7 to 2.6, and covered a complete quadrant in ϕ. Each photon was treated as a separate event, and no attempt was made to simulate the effects of pileup resulting from underlying minimum-bias events.

2 Simulation and reconstruction details

2.1 Endcap calorimeter simulation

The geometry of the endcap is described in detail elsewhere [2]. Briefly, the design uses a single crystal shape to build up a quasi-pointing calorimeter. Groups of crystals are assembled into 5×5 modules called "supercrystals", which are then used to build up the complete endcap. All of the crystals point beyond the interaction region, so that there are no pointing gaps, aside from the inter-quadrant spaces on the X and Y axes.

The crystals making up a single supercrystal are held in an alveolar container made of a rigid material, providing mechanical support and protection for the fragile lead tungstate crystals.

The simulations described here were carried out over a period of some months, during which time the design of the calorimeter was changing in many respects. The "standard" configuration used here therefore differs from the final design in several ways; most importantly in the size of the endcap crystals and the material used for the alveolar container. In the standard configuration, the container is made of glass-fibre composite material; the rear face of the crystals is $25 \times 25\text{mm}^2$. It will be clear from the results shown in this note that these differences do not invalidate the results presented here.

The crystal spacing in the standard configuration matches the final design: the distance between adjacent crystal faces is 0.5mm, of which 0.4mm is occupied by glass-fibre walls. The supercrystals are separated by a further 0.5mm air gap.

In each set of simulations, a single design parameter was varied, while all of the others were held at the standard values.

2.2 Endcap preshower simulation

The preshower simulation package described in [3] was used. The preshower detector comprises (outwards from the centre of CMS): a $2.5X_0$ lead/iron absorber; a plane of silicon strips; a $1X_0$ lead/iron absorber; and a second plane of silicon strips. The whole assembly is surrounded by neutron absorbers. The silicon strips sample the energy of electromagnetic showers, and provide positional information with a typical precision of 300μm in X and Y for photons of energy 50 GeV [4].

Like the endcap cxalorimeter, the preshower design has evolved while this work was in progress, and the latest design differes slightly from that just described. The most important difference is that the first lead absorber is now $2X_0$ in depth instead of $2.5X_0$.

2.3 Reconstruction of endcap clusters

The cluster-finding algorithm used in this study is very simple; the crystal containing the largest energy deposit is identified, and the cluster is defined as the 5×5 square array of crystals centred on this crystal. The energy of the incident photon is estimated by combining the energy deposited in the crystals with information from the endcap preshower detector described above.

For the purposes of the energy correction, the 5×5 cluster is partitioned in the manner shown in figure 2. Two correction algorithms are used, one based on the crystals only, and one using additional information from the preshower. The preshower covers the rapidity range[4] $1.65 \leq \eta \leq 2.61$, while the endcap calorimeter extends from $\eta = 1.48$ to $\eta = 3.0$. Thus, many photons striking the calorimeter have no associated preshower information. In addition, a small proportion of photons which do enter the preshower acceptance deposit a negligible amount of energy in the active material. This is illustrated in figure 3, which shows the energy deposition in the two preshower planes from photons in the range $1.7 \leq \eta \leq 2.6$.

In events with at least 5MeV and 10MeV deposited in the first and second preshower planes respectively,

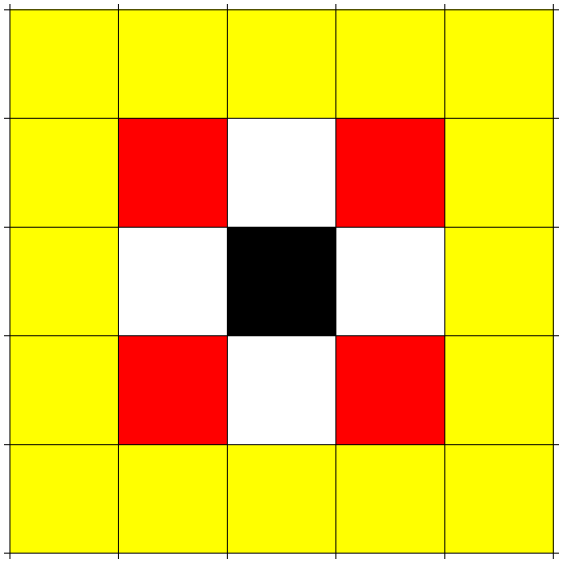

Figure 2: Cluster partitions used in energy correction algorithm. The shaded regions show the centre crystal (black), the four nearest neighbours (white), the four diagonal neighbours (dark shading), and the outer "ring" (light shading).

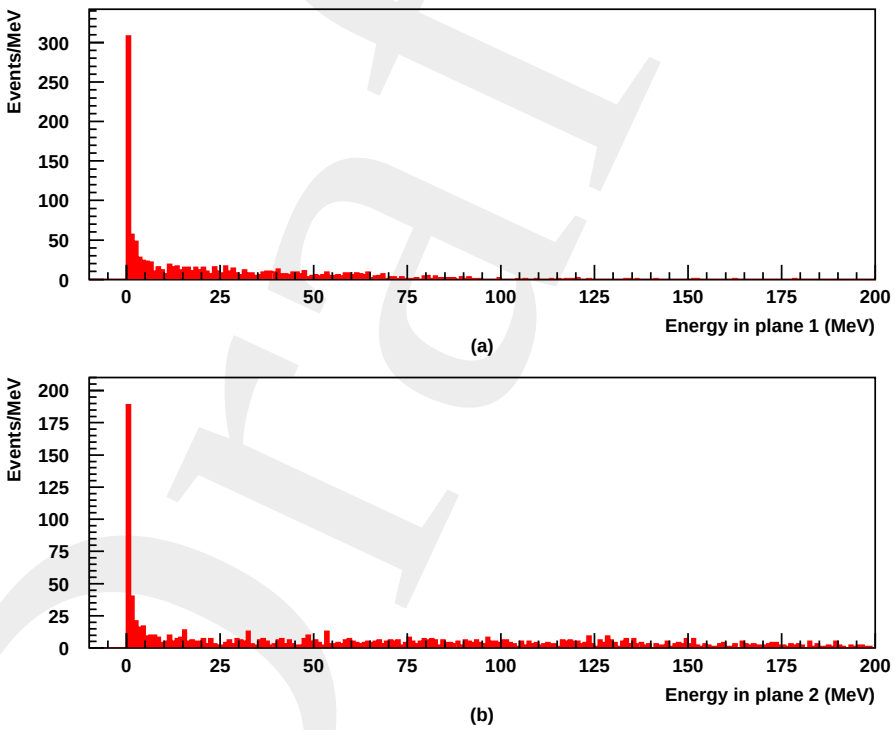

Figure 3: Energy deposition in the first (a) and second (b) silicon preshower planes for photons with $1.7 \leq \eta \leq 2.6$.

the corrected energy is given by

$$E_{corr} = a_1 E_c + a_2 E_n + a_3 E_d + a_4 E_o + a_5 P_1 + a_6 P_2,$$

where E_c, E_n, E_d, and E_o are the energies deposited in the *centre*, *nearest neighbour*, *diagonal neighbour*, and *outer* regions respectively, using the definitions shown in figure 2, and P_j is the energy deposited in preshower plane j. If the preshower energy is below threshold, either because the event was outside the preshower acceptance, or because the incident photon passed through without losing energy, the corrected energy is given by

$$E_{corr} = b_1 E_c + b_2 E_n + b_3 E_d + b_4 E_o.$$

The parameters a_i and b_i are determined by minimising the quantity

$$S^2 = \sum_k (\frac{E_{true} - E_{corr}}{E_{true}})^2,$$

where the index k runs over all events in a calibration data set.

2.4 Calorimeter performance

The principal figures of merit used to assess the performance are the energy resolution and the fraction of events in the low-energy "tail", whose reconstructed energy lies below the main Gaussian peak. These concepts are illustrated in figure 4(a), which shows the ratio of the corrected to the true energy for a sample of events using the standard endcap geometry. Most of the events fall into the main peak; the standard deviation of this peak gives the calorimeter resolution. A significant tail of events is visible below the peak. The tail fraction $f_{tail}(\xi)$ is defined as

$$f_{tail}(\xi) = N(\xi)/N_{tot},$$

where N_{tot} is the total number of events in the sample, and $N(\xi)$ is the number of events with reconstructed energy E_{corr} less than $\xi \times E_{true}$. Figure 4(b) shows $f_{tail}(\xi)$ as a function of ξ for $0.9 < \xi < 1.0$. In the remainder of this note, the expression f_{tail}, with no explicit energy fraction ξ specified, will always refer to $f_{tail}(0.98)$.

3 Effect of inter-crystal gaps

The endcap design allows gaps of 0.5mm between crystal faces within a supercrystal, with a further 0.5mm between supercrystals. In practice, the tolerance on the crystal dimensions will produce physical gaps somewhat larger than this. In this section, the calorimeter response is studied as a function of these gaps.

The reconstructed energy distributions are shown in figure 5 for inter-crystal gaps ranging from 0.5 to 0.8mm. In each case, the gap between supercrystals is the standard 0.5mm. Visually these distributions are very similar, indicating that the variation in gap has only a subtle effect on the calorimeter performance. This is confirmed quantitatively by figure 6, which summarises the behaviour of the energy resolution and the low-energy tail as functions of the gap size. Both variables show a slight trend towards worsening performance as the gaps increase, but there is no indication of a step or other discontinuity at any gap size. Both data sets are well-represented by straight lines as follows;

$$\sigma_E/E = (0.12 + 0.75 \times 10^{-3} g)\%, \text{and}$$

$$f_{tail} = (-8.0 + 0.033 g)\%,$$

where g is the size of the inter-crystal gap in μm.

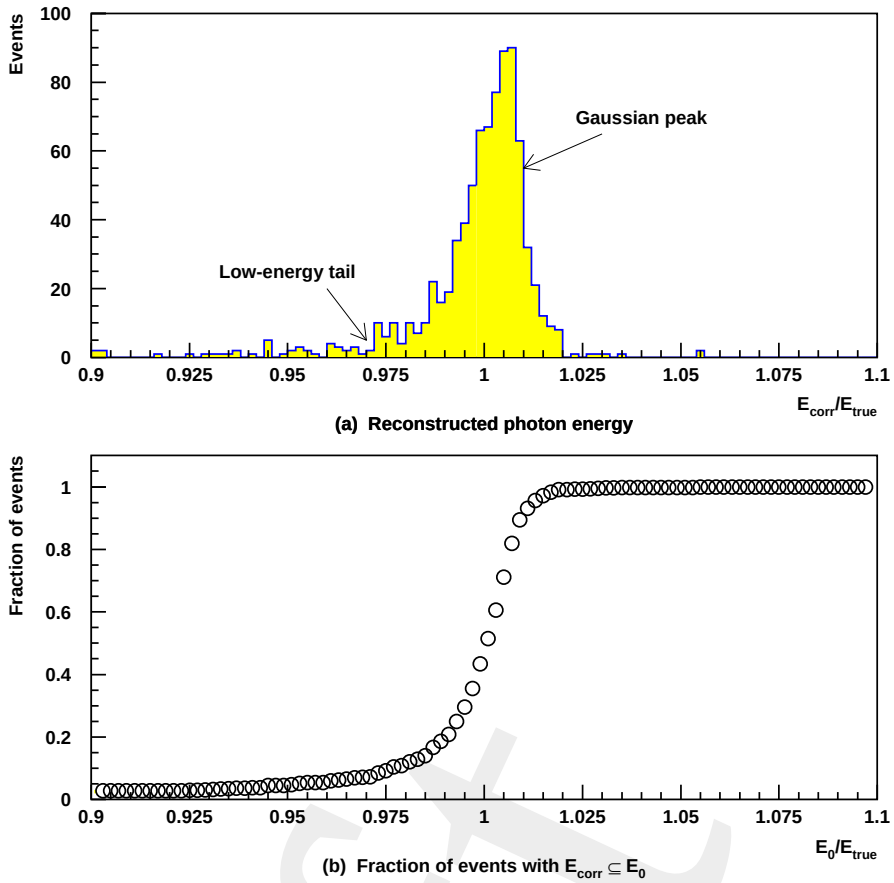

Figure 4: (a) Distribution of E_{corr}/E_{true} for standard endcap configuration.(b) Fraction of events with $E_{corr} < \xi E_{true}$ as a function of ξ.

4 Effect of inter-module cracks

The cracks between supercrystals in a column are tapered, as illustrated in figure 7. In the standard design, the front and rear gaps have the values

$$g_1 = 0.5\text{mm}, g_2 = 1.0\text{mm}.$$

The sensitivity of the calorimeter performance to changes in the crack size has been studied by generating events with the following modifications to the standard geometry.

- $g_1 = 0.8, g_2 = 1.0$
- $g_1 = 1.0, g_2 = 1.0$
- $g_1 = 1.0, g_2 = 2.0$
- $g_1 = 2.0, g_2 = 4.0$

The cracks between columns are determined by the criterion that adjacent supercrystals must be spaced at least 0.5mm apart. These cracks have a rather complicated shape determined by the stacking geometry of the calorimeter, and in this study they have not been varied.

The reconstructed energy distributions are shown in figure 8 for the crack sizes listed above.

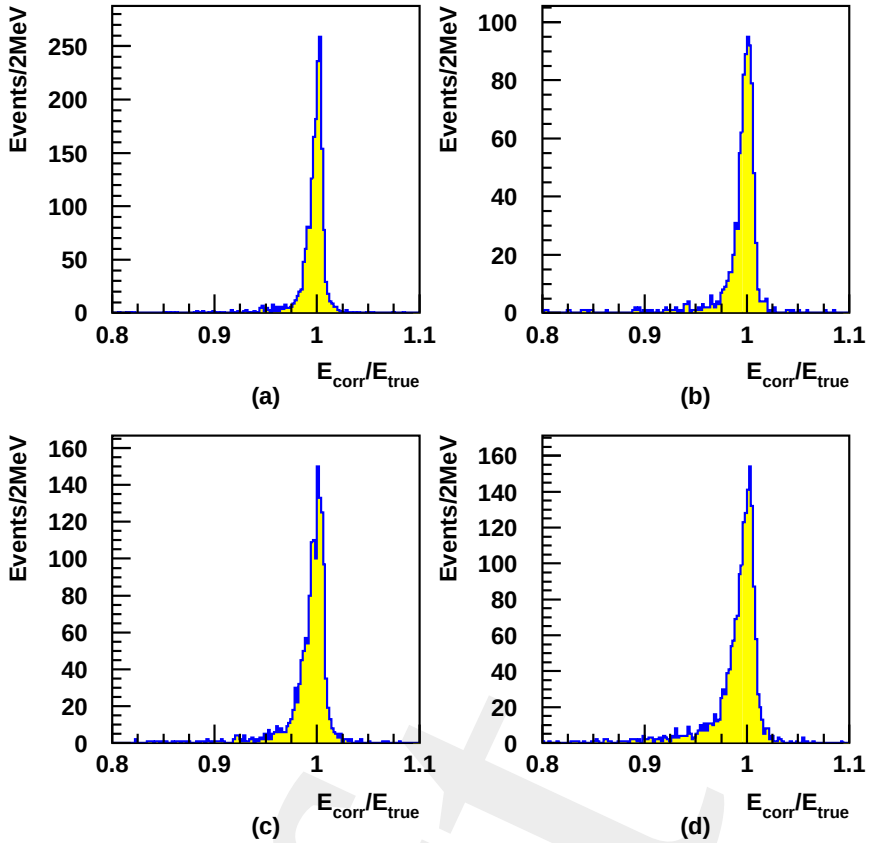

Figure 5: Distribution of E_{corr}/E_{true} for varying inter-crystal gaps: (a) 0.5mm, (b) 0.6mm, (c) 0.7mm, (d) 0.8mm.

The energy correction was tuned to achieve the best performance in each case. The energy resolution in the Gaussian peak varies little with crack size, but the low-energy tail shows a significant variation. Figure 9 shows the variation in the tail fraction as a function of g_1. The tail fraction increases approximately linearly with g_1, while g_2 appears to have a much smaller effect. There is no indication of any threshold in g_1 corresponding to a sudden change in the calorimeter performance.

5 Effect of changing the crystal size[1)]

The initial endcap design studies assumed that the crystals would be $25 \times 25\text{mm}^2$ at the rear, tapering to a smaller size at the front. A larger crystal ($25.9 \times 25.9\text{mm}^2$) was then proposed, and the final decision was to use a still larger crystal of $30 \times 30\text{mm}^2$. This section explores the effect of these changes on the calorimeter response.

A range of sizes from $25 \times 25\text{mm}^2$ to $35 \times 35\text{mm}^2$ has been simulated, in each case using the standard inter-crystal and inter-supercrystal spacing. Figure 10 shows the corrected energy distributions for each crystal size. These plots indicate that a similar performance can be achieved over the whole range of sizes; this impression is borne out by figure 11, which shows the behaviour of the peak resolution and the low-energy tails as a function of crystal size. No systematic variation is seen in either variable.

[1)] This part of the study was carried out in collaboration with H. F. Heath of Bristol University, UK

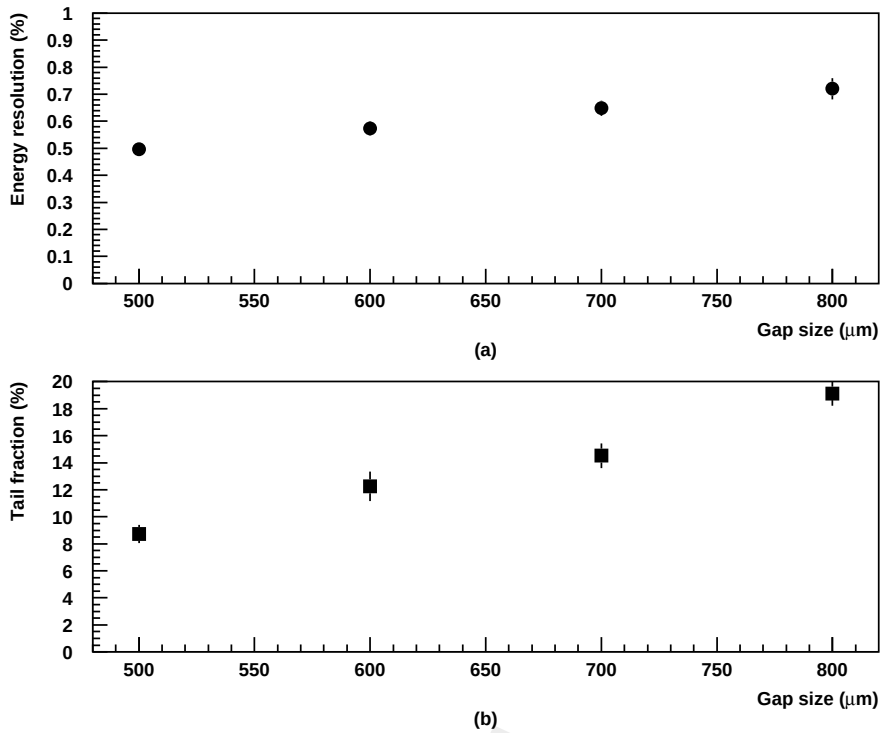

Figure 6: (a) Variation of σ_E/E with inter-crystal gap. (b) Variation of f_{tail} with inter-crystal gap.

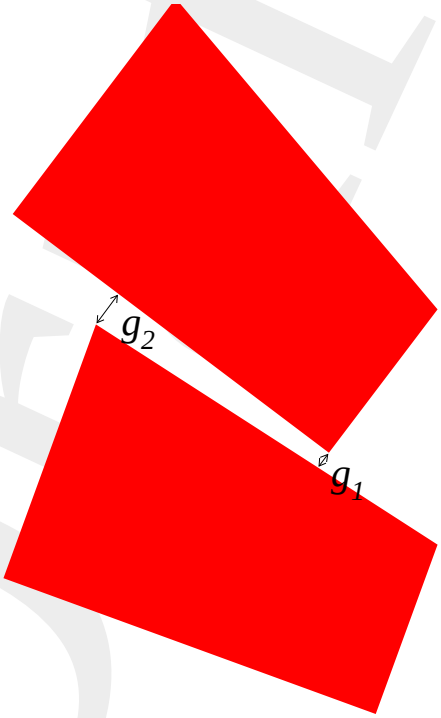

Figure 7: Schematic view of stacked supercrystals within a column, showing tapering crack.

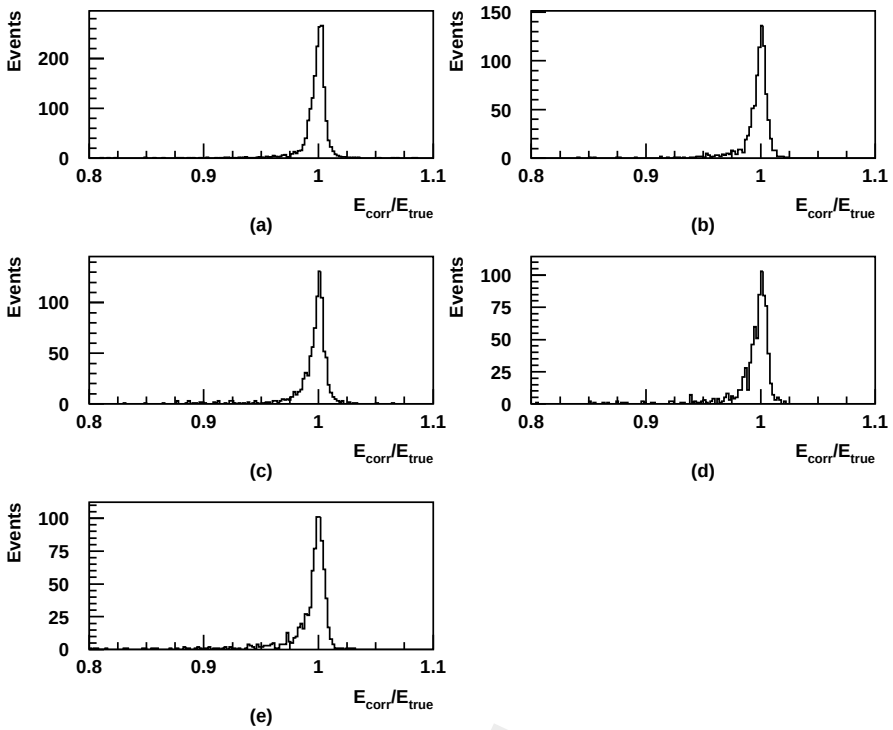

Figure 8: Distribution of E_{corr}/E_{true} for varying inter-supercrystal cracks: (a) 0.5mm front, 1.0mm rear, (b) 0.8mm front, 1.0mmrear, (c) 1.0mm front and rear, (d) 1.0mm front, 2.0mm rear, (e) 2.0mm front, 4.0mm rear.

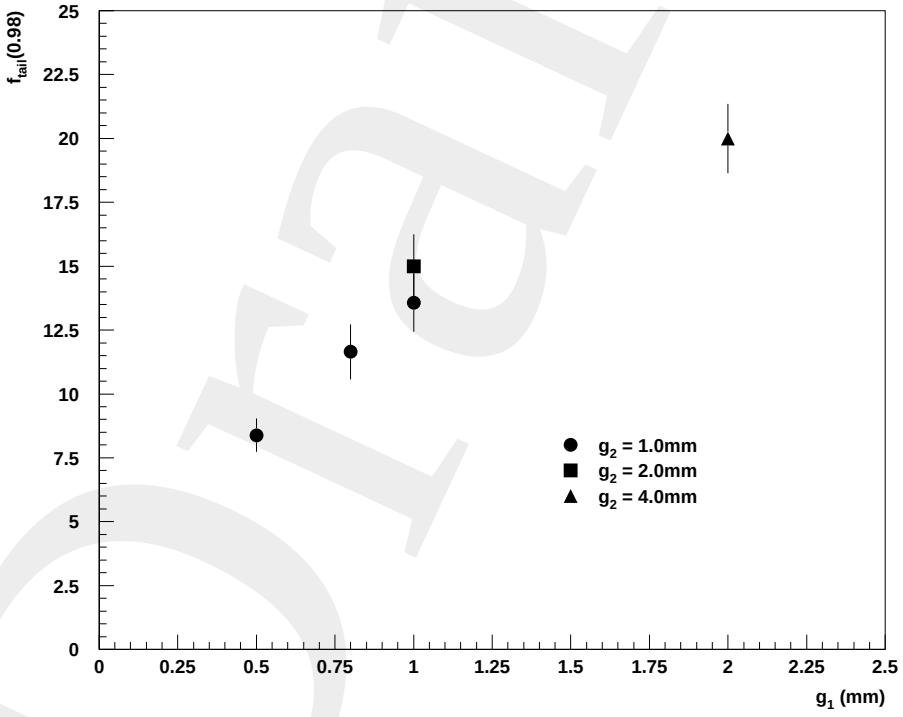

Figure 9: Variation of f_{tail} with crack size.

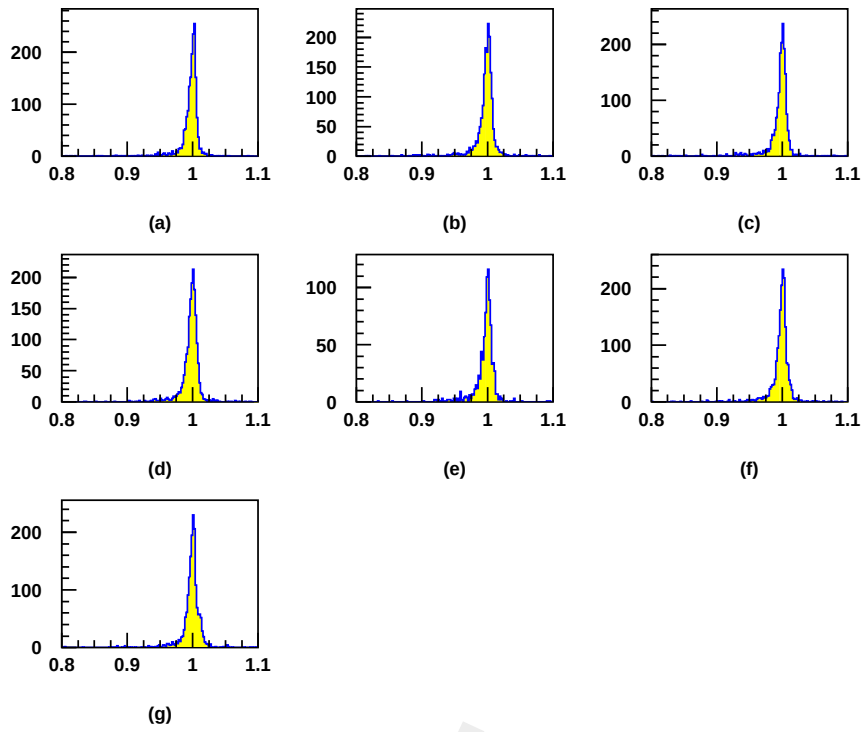

Figure 10: Distribution of E_{corr}/E_{true} for varying crystal size: (a) 25mm, (b) 27mm, (c) 28mm, (d) 29mm, (e) 30mm, (f) 32mm, (g) 35mm.

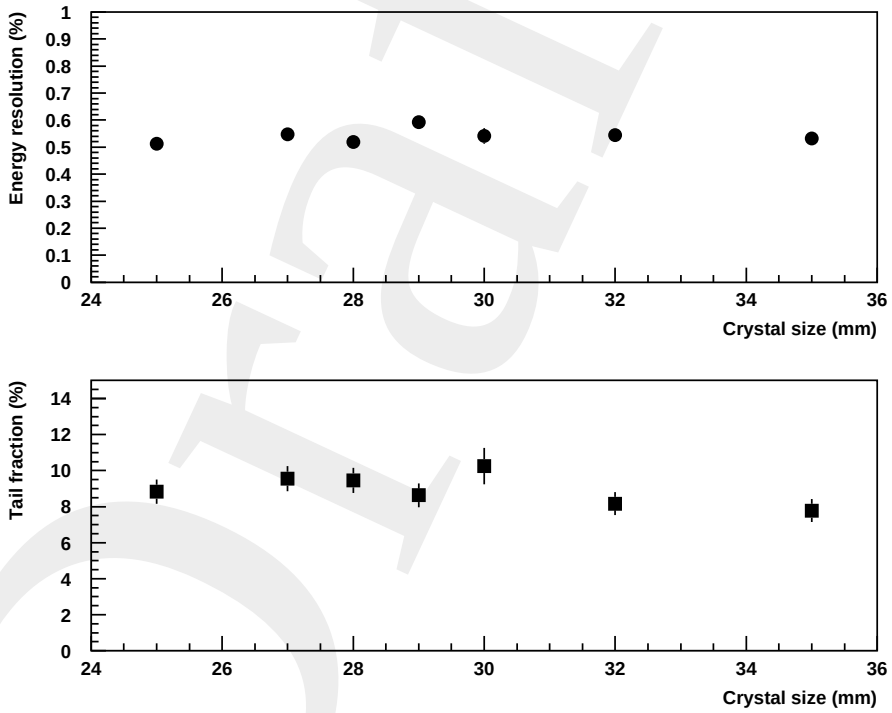

Figure 11: (a) Variation of σ_E/E with crystal size. (b) Variation of f_{tail} with crystal size.

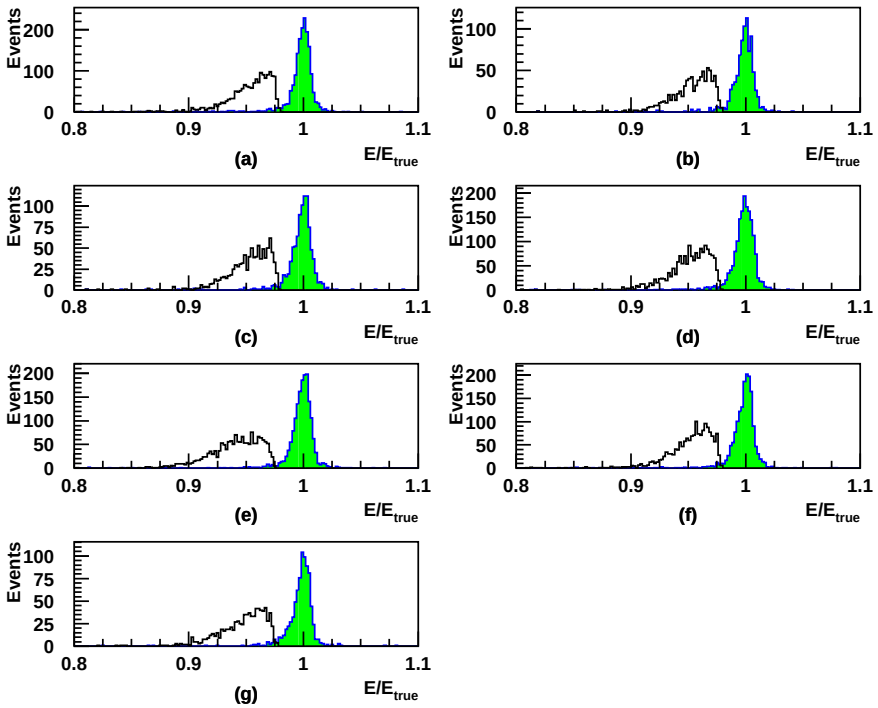

Figure 12: Distribution of E_{corr}/E_{true} (shaded) and E_{55}/E_{true} (open) for various alveolar materials (400μm-thick walls unless stated): (a) glass fibre, (b) carbon fibre, (c) aluminium, (d) steel, (e) 200μm steel, (f) titanium, (g) 200μm titanium.

6 Influence of the alveolar container material[2)]

Because of the fragility of lead tungstate, the alveolar container which holds the crystals must be strong and rigid, as well as affordable. This section assesses the impact of various possible structural materials on the calorimeter performance.

In addition to the glass-fibre alveolar containers used as the standard, the following materials have been studied: carbon fibre, aluminium, steel; and titanium at 0.4mm wall thickness; and steel and titanium only at a thickness of 0.2mm (with the total inter-crystal spacing held at 0.5mm in each case).

Figure 12 shows the raw and corrected energy distributions for each material. The distributions all look very similar, suggesting that the material used for the alveolar walls has little effect on the detector performance.

The corrected energy resolution and the size of the low-energy tail for each material option are shown in figure 13 These results confirm that the influence of the wall material is very subtle. Steel walls degrade the resolution to 0.68% compared to 0.54% for glass-fibre, and there is some indication that 400μm aluminium or titanium walls also produce a slight worsening in resolution, but the effect is of marginal significance with the current statistical errors.

7 Choice of off-pointing geometry

The shape of the endcap crystals is defined in terms of an off-pointing distance, as illustrated in figure 14. If the off-pointing distance Δz is positive, the crystal axis points beyond the interaction point. The

[2)] This work was carried out in collaboration with G. N. Patrick of RAL, UK

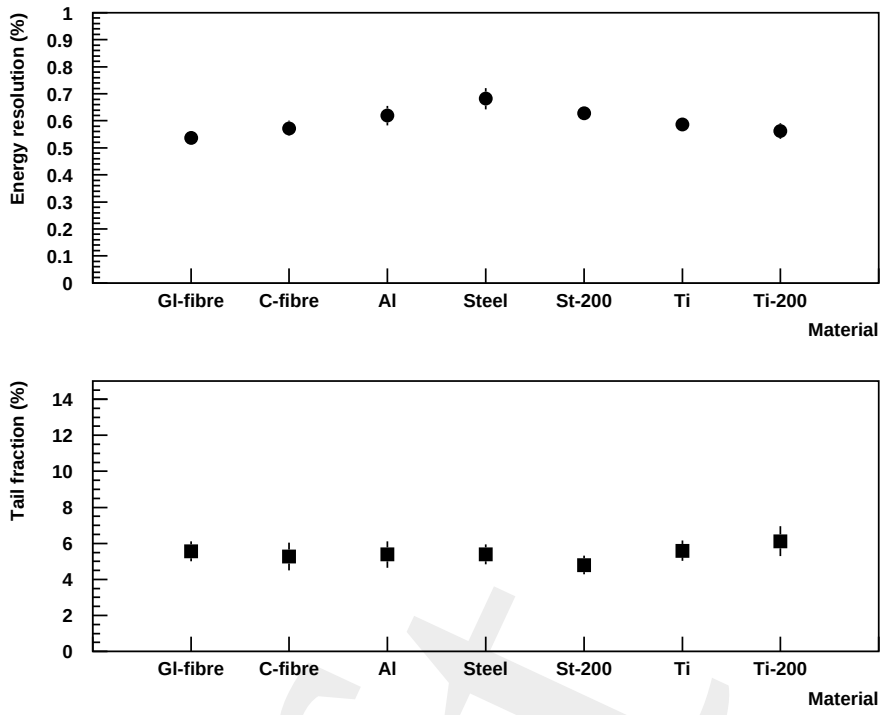

Figure 13: (a) Variation of σ_E/E with alveolar material. (b) Variation of f_{tail} with material.

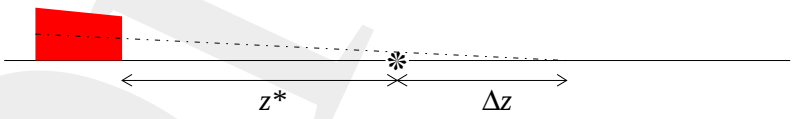

Figure 14: Definition of the endcap crystal geometry. z^* is the distance from the ECAL endcap to the interaction point, and Δz is the off-pointing distance controlling the taper.

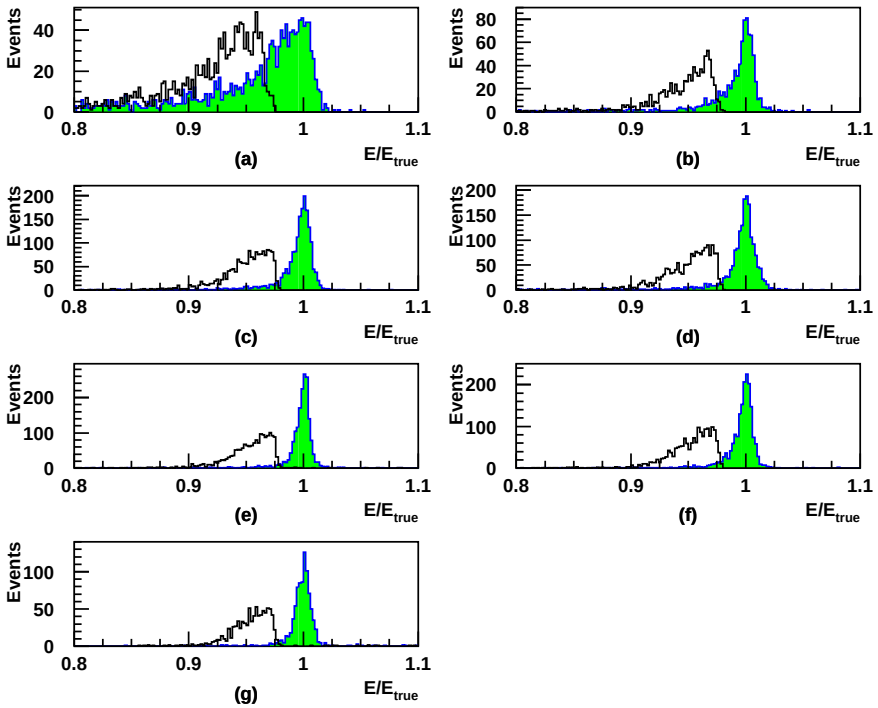

Figure 15: E_{corr}/E_{true} (shaded) and E_{55}/E_{true} (open) distributions for various values of the off-pointing distance Δz. (a) -1500mm, (b) -500mm, (c) 0, (d) 500mm, (e) 1500mm, (f) 3000mm, (g) parallel crystals.

optimal choice of Δz represents a balance between two opposing effects. If Δz is small, then the inter-crystal cracks point close to the interaction point and energy can leak out between the crystals; this tends to worsen the energy resolution and the low-energy tail. Conversely, if Δz is large the leakage is reduced, but the electromagnetic shower will spread over a larger number of crystals, again having an adverse impact on the resolution. For this study, the following range of Δz values has been used: -1500mm, -500mm, 0, 500mm, 1500mm, 3000mm, and 100m (i.e. effectively parallel-sided crystals).

Figure 15 shows the distribution of E_{55}/E_{true} and E_{corr}/E_{true} for each Δz, where E_{55} is the total energy deposited in the 5×5 crystal array described in section 2.3. Generally Δz seems to have a rather slight effect on the calorimeter performance, except for $\Delta z = -1500$mm, where both the raw and corrected energy distributions are very broad. In this configuration the effective depth of the endcap is reduced because many of the photons are incident on the sides of the supercrystals rather than the fronts, and there is substantial leakage of energy through the back of the calorimeter.

Figure 16 summarises the calorimeter performance as a function of Δz. The energy resolution in the main peak is a weak function of Δz, showing a broad minimum between 1000mm and 3000mm. The tail fraction varies in a similar manner, showing a marked deterioration at negative Δz.

8 Summary and conclusions

A variety of design options for the ECAL endcap have been evaluated in terms of their effect on the energy resolution of the calorimeter, using isolated single photons typical of those produced in the $\gamma\gamma$ decay of a light Higgs boson.

The inter-crystal gaps and the inter-supercrystal cracks are a compromise between the need for a detector which can be manufactured within financial and engineering constraints, and the physics requirement to

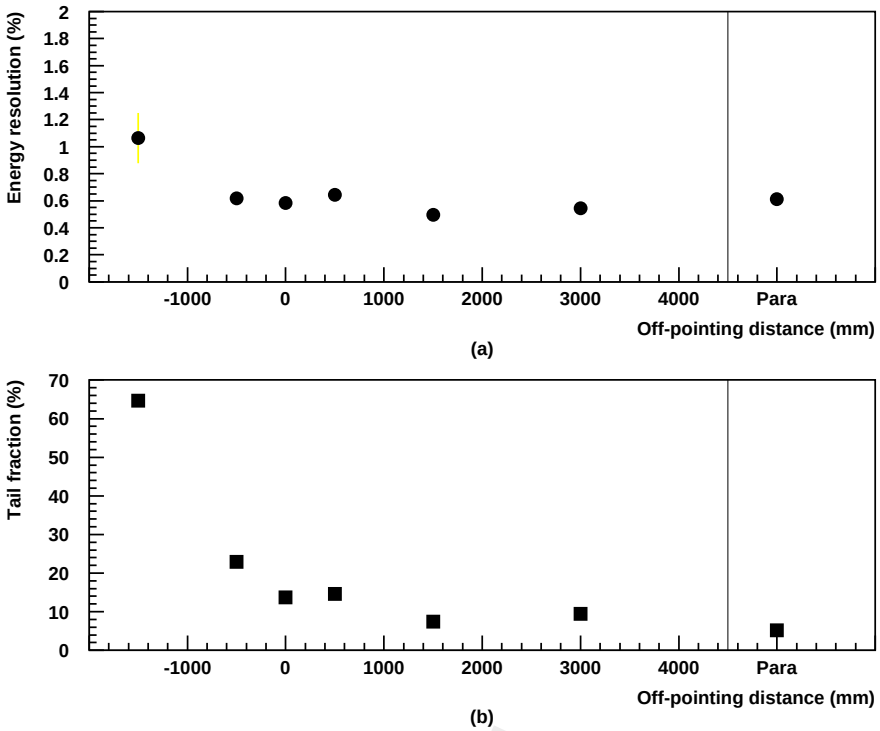

Figure 16: (a) Variation of σ_E/E with Δz. (b) Variation of f_{tail} with Δz.

avoid undue energy leakage. The nominal gap size between crystals is 500μm; section 3 showed that increasing this spacing up to 800μm has a small effect on the energy resolution, but increases the low-energy tail substantially, so that every effort must be made to space the crystals as closely as practicable.

In section 4, changing the spacing between supercrystals was found to have a much smaller effect on the calorimeter performance. Doubling the front gap to 1mm produced only a small increase in the low-energy tail, and had a negligible effect on the resolution.

Similarly, in section 5 the calorimeter performance was shown to be largely independent of the crystal size, over the range from 25×25mm^2 to 35×35mm^2. The choice of 30×30mm^2 for the final design was based on the desire to minimise the number of channels in the detector; this is the largest size of crystal which can be manufactured reliably by the suppliers.

During the endcap design period, several materials were considered for the supermodule alveolar structures. Section 6 showed that the choice of material had little effect on the physics performance, and the final selection of a carbon-fibre composite was based on engineering and cost considerations.

Finally, section 7 examined the off-pointing geometry of the endcap, parameterised by the distance Δz beyond the interaction region to which the crystals pointed. The calorimeter performance was found to vary little for Δz in the range 1000-3000mm. The actual choice of $\Delta z = 1370$mm lies comfortably within this broad optimal region.

References

[1] B. W. Kennedy, CMS TN/96-043, 18 March 1996

[2] B. W. Kennedy, note in preparation

[3] D. Barney, CMS IN 1997/015, 14 May 1997

[4] The CMS ECAL TDR, CERN/LHCC 97-33, 15 December 1997.